ELSEVIER

Journal of Fluids and Structures 21 (2005) 49–64

JOURNAL OF FLUIDS AND STRUCTURES

www.elsevier.com/locate/jfs

Fluid dynamics around an inclined cylinder with running water rivulets

Z.J. Wang[a], Y. Zhou[a,*], J.F. Huang[a], Y.L. Xu[b]

[a]*Department of Mechanical Engineering, The Hong Kong Polytechnic University, Hung Hom, Kowloon, Hong Kong*
[b]*Department of Civil and Structural Engineering, The Hong Kong Polytechnic University, Hung Hom, Kowloon, Hong Kong*

Received 20 September 2004; accepted 6 May 2005
Available online 13 September 2005

Abstract

The formation of water rivulets running along an inclined circular cylinder and its effects on the near-wake were experimentally investigated. Water was released from the upper end of the cylinder at a volume flow rate Q. At an incoming wind speed $U_\infty = 8-15\,\mathrm{m/s}$, two water rivulets were observed near the flow separation points, running along the cylinder inclined at $\alpha = 45^\circ$ for $0^\circ \leqslant \beta \leqslant 90^\circ$, where β is the cylinder yaw angle, and both oscillating circumferentially. The dependence of the rivulet formation on U_∞, Q and β is examined in detail. The quasi-periodic vortex street is observed intermittently with and without the presence of the rivulets. The rivulets cause an increase in the normalized dominant frequencies in the near wake and further lead to a significant increase in the drag coefficient, which is consistent with the violent vibration associated with the rain–wind-structure interactions. The effect of the rivulets on the near-wake vortices is investigated. It is found that the vortex strength grows by up to 60% as β increases from 0° to 30°. A mechanism for the rain–wind-induced cable vibration is proposed.

1. Introduction

Long and flexible cables in modern cable-stayed bridges are inherently of low damping and are susceptible to vibration in a cross-wind due to fluid excitation forces associated with vortex shedding from the cables. In the presence of rain, oscillating and moving water rivulets occur along a cable. The ensuing aero-hydro-elastic interaction between cable, wind and oscillating water rivulets results in a grossly amplified cable vibration within a certain range of wind speeds and restricted large vibration amplitudes. Wianecki (1979) was perhaps the first to report the rain–wind-induced vibration of stay cables associated with the Brotonne Bridge in France. Since then, the observation of the rain–wind-induced cable vibration has been reported for a number of long span bridges in many countries. The rain–wind-induced cable vibration may have maximum peak-to-peak amplitude up to 6 times the cable diameter, thus affecting the fatigue life of the cable, and even causing cable damage and affecting the safety of the entire bridge (Verwiebe and Ruscheweyh, 1998). This problem has become a great concern to bridge engineers.

Naturally, interest in understanding the mechanisms of the rain–wind-induced cable vibration has been rapidly growing in the last decade; both field measurements and wind tunnel tests with rain conditions simulated have been vigorously pursued. Hikami and Shiraishi (1988) argued that the so-called rain–wind-induced cable vibration was not a

*Corresponding author. Tel.: +852 2766 6662; fax: +852 2365 4703.
E-mail address: mmyzhou@polyu.edu.hk (Y. Zhou).

0889-9746/$ - see front matter © 2005 Elsevier Ltd. All rights reserved.
doi:10.1016/j.jfluidstructs.2005.05.017

simple vortex-induced oscillation, since the rain–wind-induced vibration was characterized by a much lower frequency but a much larger amplitude than that associated with the vortex-induced oscillations; wake galloping is also excluded because the cables are separated sufficiently far to avoid any interactions between them. Yamaguchi (1990) concluded that one-degree-of-freedom galloping theory could not explain the rain–wind-induced cable vibration, and a two-degree-of-freedom galloping theory might be required. This vibration, for most of the time, occurs for wind speeds from 8 to 15 m/s and yaw angles in the range $\beta = 20-60^{\circ}$; it is always associated with water rivulets running along the cable and oscillating circumferentially (Yoshimura et al., 1988; Flamand, 1995). In general, two water rivulets are formed, occurring on the lower windward side and upper leeward side of the cable, respectively. The upper rivulet on the leeward side is largely responsible for the rain–wind-induced cable vibration, while the other on the windward side has a negligible effect (Ohshima, 1987; Hikami and Shiraishi, 1988; Flamand, 1995; Bosdogianni and Olivari, 1996). The reports in the literature are not always consistent with each other. For example, while many observations of the rain–wind-induced vibration were made at a yaw angle, mostly near 45°, Verwiebe and Ruscheweyh (1998) reported the damage of nearly vertical steel bars of a new bridge due to the rain–wind-induced vibration. Flamand (1995) conducted full-scale wind tunnel tests and observed the rain–wind-induced cable vibration. Once the moving rivulets were replaced by false fixed rivulets glued on the cable surface, he could not observe the rain–wind-induced vibration. He concluded that the oscillation of the upper water rivulet played a crucial role for the generation of the rain–wind-induced vibration. The same opinion was shared by Verwiebe and Ruscheweyh (1998). The latter authors further interpreted that the oscillation of water rivulets resulted in a variation in the cable cross-sectional shape and hence in the pressure distribution around the cable. Consequently, the resultant force on the cable was varying and exciting the cable. On the other hand, Bosdogianni and Olivari (1996) used two bars of various shapes to simulate the water rivulets and observed a strong increase in the oscillation amplitude of the cable. Therefore, they contested that it was the protuberances at certain positions on the cable surface that caused the rain–wind-induced vibration, and the oscillation of water rivulets or the shape of the simulated rivulets had little or no influence on the instability. Matsumoto et al. (1995) proposed three types of rain–wind-induced cable vibration, namely, the "galloping" type, the vortex-shedding type, and a combination of both. The vortex-shedding type was characterized by a period longer than the classical Karman vortex shedding. The galloping type included both divergent galloping and velocity-restricted galloping. They further linked the velocity-restricted galloping to the three-dimensionality of the Karman vortex. Based on the power spectrum of the lift force and flow visualization, Matsumoto et al. (2001a) proposed that the fluid interaction between Karman vortex and axial vortex could be responsible for the rain–wind-induced cable vibration.

Previous work has greatly improved our understanding of the rain–wind-induced cable vibration. This understanding has guided the development of a number of techniques in bridge engineering to alleviate the problem; for example, increasing the damping by using damping ropes between the cables, dynamic vibration absorbers, and dashpots at the cable footing, deflecting water on the cable surface, or preventing the water rivulets from oscillating circumferentially. However, these techniques are far from adequate, probably because many aspects of the rain–wind-induced vibration have yet to be clarified, including its generation mechanisms (Matsumoto et al., 2001b). Existing investigations mostly focused on engineering issues such as how, when and where the problem occurs and how to prevent the problem from occurring; there does not seem to have been a systematic research on the fundamental aspects of this important engineering problem, especially on the fluid dynamics associated with this problem, in spite of the fact that the rain–wind-induced vibration originates from the fluid excitation force. There has been a wealth of papers in the literature with regard to the wake of a yawed stationary or oscillating cylinder (Thomson and Morrison, 1971; Ramberg, 1983). It is the flow behind the yawed cylinder (both stationary and oscillating) with running water rivulets that needs more attention. Matsumoto et al. (2001a) have identified the importance of axial-flow/vortices in the generation of the rain–wind-induced vibration. But the axial-flow/vortex mechanism is not entirely clear (Matsumoto et al., 1998). A number of other issues can also be crucial to understand thoroughly this problem. How does the occurrence of water rivulets affect the near-wake fluid dynamics of the cable, including the vortex formation process, dominant frequency, flow structure and downstream evolution? How do the water rivulets and their oscillation change the coupling between fluid dynamics and structural dynamics? These issues warrant an in-depth investigation on fluid dynamics, structural dynamics and their nonlinear coupling and motivate the present study.

This work aims to improve our understanding of the fluid dynamics associated with an inclined stationary cylinder with running water rivulets, and to develop our understanding of the effects of water rivulets on the near-wake fluid dynamics. Specifically, it is undertaken to measure and compare the near-wake of an inclined cylinder, with and without the presence of water rivulets; investigate the three dimensional characteristics of the flow around the cylinder, especially interactions between Karman vortices and longitudinal structures. The nonlinear coupling between fluid dynamics and structural dynamics associated with the rain–wind-induced cable vibrations will be investigated in subsequent work. Experimental details are given in Section 2. The experimental results are presented and analyzed in Sections 3–5. The work is concluded in Section 6.

2. Experimental details

2.1. Experimental setup

Experiments were carried out in a closed circuit wind tunnel with a working section of $L \times W \times H = 2.4\,\text{m} \times 0.6\,\text{m} \times 0.6\,\text{m}$. The view window of the working section was made of optical glass in order to maximize the signal-to-noise ratio. The maximum wind speed in the working section was 50 m/s and the longitudinal turbulence intensity was approximately 0.4%. The cable was modeled by a rigid polyethylene-lapped acryl glass tube of 0.6 m in length (for such a length, even the real flexible cables would be rather rigid). Its surface condition is similar to that associated with the real cables. Two cable models were used in the present investigation, one with an external diameter, d, of 45 mm and the other 19 mm, resulting in aspect ratios of 13.3 and 31.6, respectively. The corresponding blockage was 7.5% and 3.2%, respectively. The size of the larger diameter model falls in the range of actual cables, with improved accuracy in identifying the rivulet position on the model surface. This model was mainly used to examine the behavior of water rivulets. Our measurements indicated that the patterns of the formed rivulets are almost identical along most of this model, thus suggesting a negligible aspect ratio effect on the rivulets around the mid-span of the model. On the other hand, the smaller diameter model had negligible blockage and end effects, and it was used to investigate the detailed flow structures. The end plates were used to minimize further the possible aspect ratio effect (see Fig. 1).

The experimental arrangement is schematically shown in Fig. 1. The cable model was supported as a cantilever. The top end of the cylinder was connected to a small turning plate mounted on the ceiling of the working section through a hinge, so that the inclination α and yaw angle β of the cylinder can be adjusted to simulate all possible directions of the wind. The angles of α, β, and θ (the circumferential angle) are defined in Fig. 2. The x-axis is in the same direction as the incoming wind velocity, the y-axis is perpendicular to the x-axis in the horizontal plane, and the z-axis is normal to both x and y. The origin of the coordinate system is defined at mid-span of the model axis. The angle $\theta = 0^\circ$ is designated as the major axis on the leeward side of the elliptical cross section A–A′ in the (x, y)-plane. In order to identify the rivulet position, a red grid was marked on the cylinder surface with a circumferential increment of 10° and a spanwise increment of 50 mm. The grid lines at $\theta = 0^\circ$, $\pm 90^\circ$ and $\pm 180^\circ$ were highlighted with black color to facilitate the identification of the θ value. Water was released at the upper end of the cylinder at $\theta = 0^\circ$ from a water tank. To maintain a steady flow rate, the liquid level H_0 in the tank was maintained to be constant throughout the experiments. Four flow rates were selected: $Q = 1.4$, 3.0, 6.9 and 8.0 l/h. This was achieved by adjusting a regulator valve. The rivulets were marked by ink, and were recorded using a digital video camera (Sony DCR-PC100E) at a framing rate of 25 frames/s.

2.2. PIV and flow visualization measurements

A Dantec PIV system, introduced in detail by Xu et al. (2003), was used to measure the near wake of the inclined cylinder in both the horizontal (x, y) plane and a vertical plane through the cylinder axis. The cylinder surface and the tunnel working section wall hit by the laser sheet were painted black to minimize reflection noise. The flow was seeded by smoke, generated from Paraffin oil, of a particle size around 1 μm in diameter. Each image from the PIV measurements covered an area of $112\,\text{mm} \times 140\,\text{mm}$, i.e. $x/d = 1 \sim 6.9$ and $y/d = \pm 3.7$ ($d = 19\,\text{mm}$). The cylinder, included in the PIV images, was masked using a built-in masking function in the PIV system before particle velocities were calculated. In image processing, 32×32 rectangular interrogation areas were used with 25% overlap in each direction. The ensuing in-plane velocity vector field consisted of 53×42 vectors, based on which approximately the same number of vorticity data-points were obtained. The spatial resolution for vorticity estimate was about $0.14d$. The PIV measurements were conducted at $U_\infty = 9\,\text{m/s}$ and $Q = 8.0\,\text{l/h}$ for $\alpha = 45^\circ$, $\beta = 0^\circ$ and 30°. The corresponding Reynolds number Re ($\equiv U_\infty d/\nu$, where ν is the kinematic viscosity of air) was 1.14×10^4. More than three hundred images were obtained for each β.

The laser-illuminated flow visualization was also conducted in the wind tunnel using the visualization function of the PIV system in order to provide the qualitative information on the flow field. The larger diameter model was used. The camera was operated in the single frame mode. The view-field was $118\,\text{mm} \times 148\,\text{mm}$, corresponding to $x/d = 1 - 7.2$ and $y/d = \pm 3.9$.

2.3. LDA measurements

The wind tunnel and other experimental conditions were the same as those used for the PIV measurements. In order to obtain the quantitative information of the rivulet effects on the near wake of the cylinder, a two-component LDA (Dantec Model 58N40 LDA with enhanced FVA signal processor) was used to measure velocities at $x/d = 3$ in the

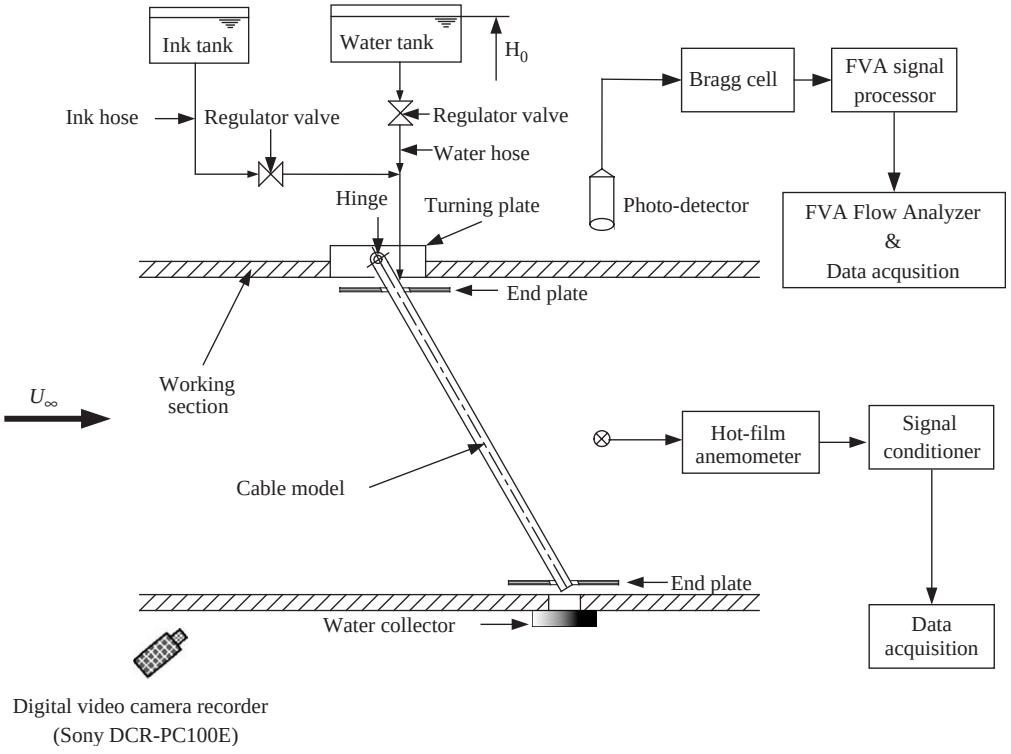

Fig. 1. Schematic of experimental arrangement.

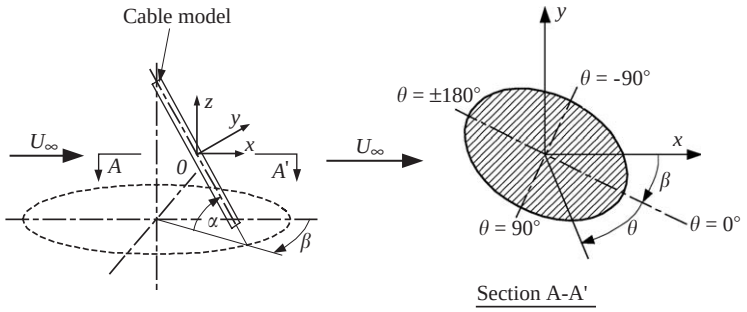

Fig. 2. Definitions of inclination angle α, yaw angle β, circumferential angle θ, and the coordinates x, y and z. The origin of the coordinate system was defined at mid span of the cable axis.

mid-horizontal plane, $z = 0$, of the working section (Fig. 1). The LDA measuring volume has a minor axis of 1.18 mm and a major axis of 2.48 mm. The measured mean velocity was estimated to have an error of less than 3% and the corresponding error for the measured root-mean-square value was less than 10%. The flow seeding was the same as used for the PIV measurement. For each data-point, 250 000 validated samples were acquired with a data rate of 0.8–4 kHz. The LDA system comes with the necessary software for data processing and analysis, and the data, besides the mean field, could be processed to yield information on the Reynolds stresses.

2.4. Hot-film measurements

The hot film was chosen to monitor the fluctuating flow velocity, instead of a hotwire, which would be vulnerable in a wind mixed with water droplets. The hot film, operated at an overheating ratio of 1.8 with a constant temperature anemometer, was placed at $x/d = 3.0$ and $y/d = -4.0-4.0$. The signal from the anemometer was offset, amplified and

then digitized using a 12-bit A/D board and a personal computer at a sampling frequency of 3.5 kHz. The duration of each record was 20 s.

3. Rivulet formation

For $90^\circ < \beta \leqslant 180^\circ$, the water, released at the upper end of the cylinder at $\theta = 0^\circ$ and running over the model surface, faced the incoming freestream velocity (refer to Fig. 2), and thus was blown away; no water rivulets being observed. In the range of $0^\circ \leqslant \beta \leqslant 90^\circ$, however, the water released at the top end of the cylinder developed into one lower (windward) and one upper (leeward) rivulet along the cylinder surface for $U_\infty = 8.0-15.0$ m/s and for all cylinder inclinations α and flow rates Q presently examined, which is consistent with previous reports (Hikami and Shiraishi, 1988; Bosdogianni and Olivari, 1996).

Fig. 3 presents typical patterns of rivulets along the cylinder at $\alpha = \beta = 45^\circ$, $Q = 8.01$/h and $U_\infty = 9.0$ m/s. Two regular rivulets were formed: one on the leeward (upper side) and the other on windward (lower) side of the cylinder. The former (Fig. 3(b)) follows a pseudo-sinusoidal wave along the cylinder with an axial wavelength of about $2d$, oscillating circumferentially; the latter (Fig. 3(a)) runs approximately in a straight line. It was found presently that the circumferential oscillation of the leeward rivulet was increased in magnitude with increasing β. For example, when β exceeded 45°, the leeward circumferential oscillation exhibited a large amplitude; a stable rivulet occurred only intermittently. As β approached 0°, however, the pattern of the leeward rivulet appeared essentially identical to that of the windward rivulet, whose pattern was approximately a straight line with a very small amplitude of circumferential oscillation, and was almost unchanged for $0^\circ \leqslant \beta \leqslant 90^\circ$ (e.g., Fig. 3(a)).

The mean circumferential position of a rivulet around the cylinder is given by θ. Based on the recorded video with the help of the grid, the windward rivulet shown in Fig. 3 is found to occur at $\theta \approx -160^\circ$, while the leeward one appears at $\theta \approx 30^\circ$. The θ value of the two rivulets varies with β, as shown in Fig. 4 for $\alpha = 45^\circ$, $Q = 8.01$/h and $U_\infty \approx 9.0$ m/s. As β approaches 90°, the leeward and windward rivulets approach $\theta = 0^\circ$ and -180°, respectively.

It is well known that, for a circular cylinder placed normal to incident velocity, flow separation occurs at about 80° from the leading stagnation point for a reasonably high Re (Chen, 1987). Interestingly, Fig. 4 shows that at $\beta = 0$ both rivulets occur at $\theta \approx \pm 110^\circ$, respectively, i.e. about 70° from the leading stagnation point. In view of the uncertainty ($\pm 5^\circ$) in determining θ and the possible effect of rivulets on the flow separation point, it may be inferred that the two rivulets are most likely to occur near the flow separation lines, probably due to a lower pressure in the flow separation region (Chen, 1987; Zhou et al., 2001). The result is consistent with the previous conjecture by Bosdogianni and Olivari (1996). Dwyer and McCroskey (1973) reported that flow separation points on a circular cylinder were not fixed but kept oscillating on the cylinder surface, and their circumferential excursion was usually within 10°, varying from 75° to 85° from the leading stagnation point, for $\mathrm{Re} = 1.06 \times 10^5$. This may explain the present observation that the water rivulets oscillated circumferentially on the cylinder surface.

It is worth commenting on the distinct geometric characteristics between the two running rivulets. The dynamic equilibrium of the water rivulets depends on a number of forces, i.e., the drag force, inertia force of water, gravity force, tension force, friction force between the rivulets and the cylinder surface, the force from the cylinder, etc. As a result, the rivulet geometric characteristics and position are dependent upon Q, α, β, cylinder surface roughness and other effects. The leeward rivulet displays a pseudo-sinusoidal wave (Fig. 3(b)). It has been reported that vortex shedding from a circular cylinder is unlikely to be in phase along the cylinder axis, in particular at a high Re; the vortex cell has a typical spanwise extent of $1-3d$ (King, 1977; Higuchi et al., 1989). This may well explain the pseudo-sinusoidal wave with an axial wavelength of about $2d$. On the other hand, the windward rivulet runs in an approximate straight line. It is speculated that this rivulet, facing downwards, tends to be more influenced by the gravity force, which might overwhelm the three-dimensional effect of vortex rolls shed from the cylinder, leading to a near-straight-line characteristic.

Fig. 5 presents the variation in the position of the leeward rivulet θ_L with β and U_∞ for $\alpha = 45^\circ$ and $Q = 8.01$/h. It is evident that θ_L tends to retreat for a higher U_∞, irrespective of the β value, indicating that this rivulet climbs up the cylinder surface. This is also the case for the windward rivulet, as will be shown in Fig. 6(b). Similar observations were made by Hikami and Shiraishi (1988) and Bosdogianni and Olivari (1996). Two causes may be responsible. Firstly, the wind force acting on the rivulet increases for a higher U_∞ and thus pushes the rivulet up. Secondly, the mean location of flow separation points may vary with Re. For example, Achenbach (1968) found experimentally that the boundary layer separation points around a circular cylinder occurred at 78° from the leading stagnation point for $\mathrm{Re} = 10^5$, but shifted to 94° for $\mathrm{Re} = 3 \times 10^5$. Accordingly, the circumferential position of the leeward rivulet varies, though very slightly with U_∞.

The θ variation of the rivulets with U_∞ was compared with Hikami and Shiraishi's (1988) data in Figs. 5 and 6. There is a good agreement in θ_w of the windward rivulet between the present measurement at $Q = 8.01$/h ($\beta = 45^\circ$) and theirs. The present data of the leeward rivulet agree qualitatively with theirs; there is appreciable deviation for small U_∞,

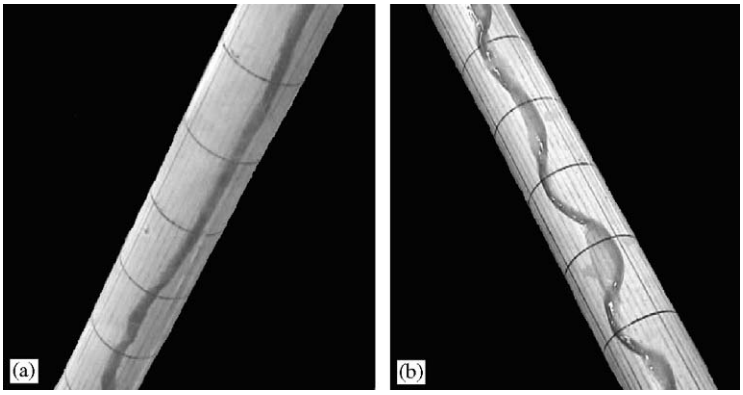

Fig. 3. Rivulets on the cylinder at $\alpha = \beta = 45^\circ$, $U_\infty = 9.0\,\mathrm{m/s}$, and $Q = 8.01/\mathrm{h}$: (a) Windward rivulet at $\theta \approx -160^\circ$; (b) leeward rivulet at $\theta \approx 30^\circ$.

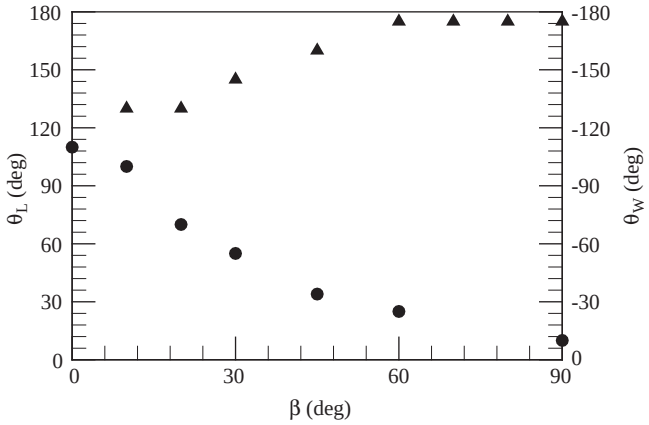

Fig. 4. Dependence of the rivulet position θ on the yaw angle β at $\alpha = 45^\circ$, $U_\infty \approx 9.0\,\mathrm{m/s}$, and $Q = 8.01/\mathrm{h}$: ●, leeward rivulet (θ_L); ▲, windward rivulet (θ_w).

particularly at $U_\infty = 9\,\mathrm{m/s}$. This discrepancy could be ascribed to the fact that the current water releasing procedure differed from actual rain conditions, where water was gradually accumulated on the cable surface [e.g., Wianecki (1979)]. On the other hand, Hikami and Shiraishi used artificial rain to form the rivulets. To clarify the effects of water mass-flow rate on the rivulet formation, Fig. 6 shows the variation in θ of the leeward rivulet with the water flow rate Q and U_∞ for $\alpha = \beta = 45^\circ$. At $U_\infty \approx 9.0\,\mathrm{m/s}$, the leeward rivulet occurs at $\theta_L \approx 26^\circ$, 28° and 34° for $Q = 1.4$, 3.0 and $8.01/\mathrm{h}$, respectively (Fig. 6(a)). The deviation in θ_L at the same U_∞ but different Q is apparently connected to the gravity force effect. For a higher U_∞, θ_L decreases, that is, the leeward rivulet climbs up towards $\theta = 0^\circ$, which is more evident at $Q = 3.01/\mathrm{h}$ than at $Q = 1.4$ and $8.01/\mathrm{h}$. At $Q = 3.01/\mathrm{h}$, θ_L is very sensitive to U_∞ at intermediate Q, rather similarly to Hikami and Shiraishi's (1988) observation that θ_L experienced a fast drop with increasing U_∞ (Fig. 6(a)). The windward rivulet position θ_w (Fig. 6(b)) displays a trend similar to θ_L for all the water rates Q used, moving towards $\theta = 0^\circ$ for higher U_∞, though slowly. This relatively slow shift is ascribed to the gravity effect, which is expected to have more influence on the windward (lower) rivulet than the leeward (upper) one.

4. Flow structure

4.1. Cross-flow distributions of mean velocities and Reynolds stresses

Figs. 7 and 8 present the LDA-measured cross-flow distributions of mean velocity $\overline{U}^*$, $\overline{V}^*$, Reynolds normal stresses $\overline{u^2}^*$ and $\overline{v^2}^*$, and shear stress $\overline{uv}^*$ measured in the (x, y) plane at $x/d = 3$ for $\beta = 0^\circ$ and 30°, respectively. In this

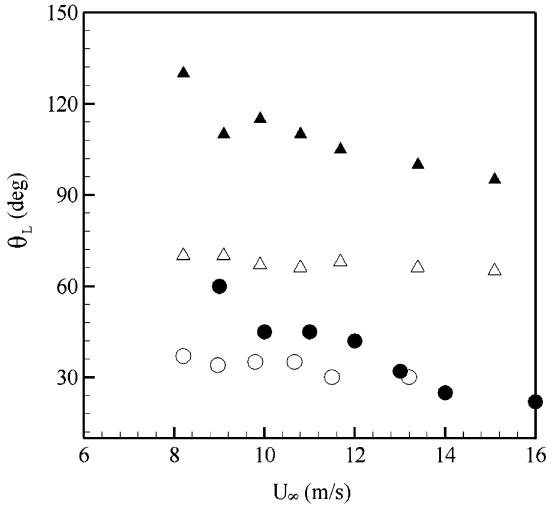

Fig. 5. Dependence of the leeward rivulet position θ_L on the yaw angle β and free-stream velocity U_∞ at $\alpha = 45^\circ$ and $Q = 8.01$/h: ▲, $\beta = 0^\circ$; △, $\beta = 20^\circ$; ○, $\beta = 45^\circ$; ●, $\beta = 45^\circ$ [artificial rain, Hikami and Shiraishi (1988)].

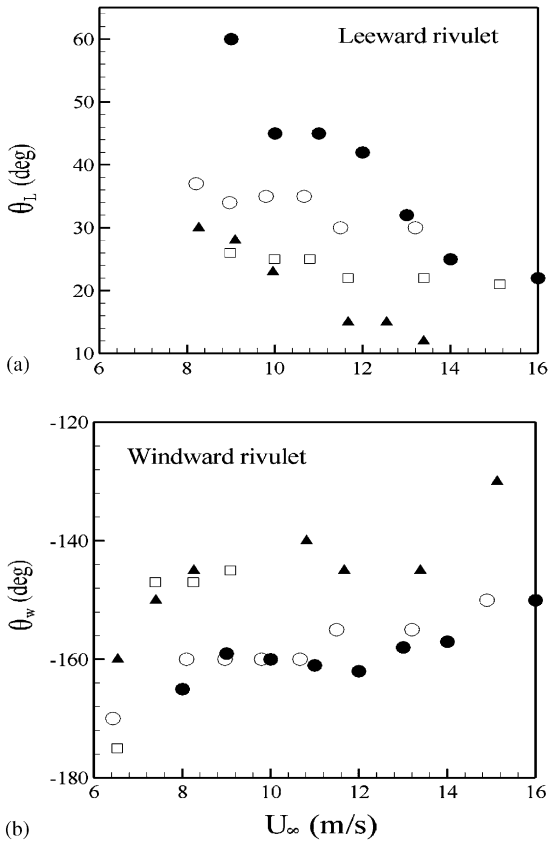

Fig. 6. Dependence of the rivulet position θ on the water releasing rate Q and the free stream velocity U_∞ at $\alpha = \beta = 45^\circ$: (a) leeward rivulet θ_L; (b) windward rivulet θ_w. □, $Q = 1.41$/h; ▲, $Q = 3.01$/h; ○, $Q = 8.01$/h; ●, $\beta = 45^\circ$ [Hikami and Shiraishi (1988), where water rivulets were formed from artificial rain].

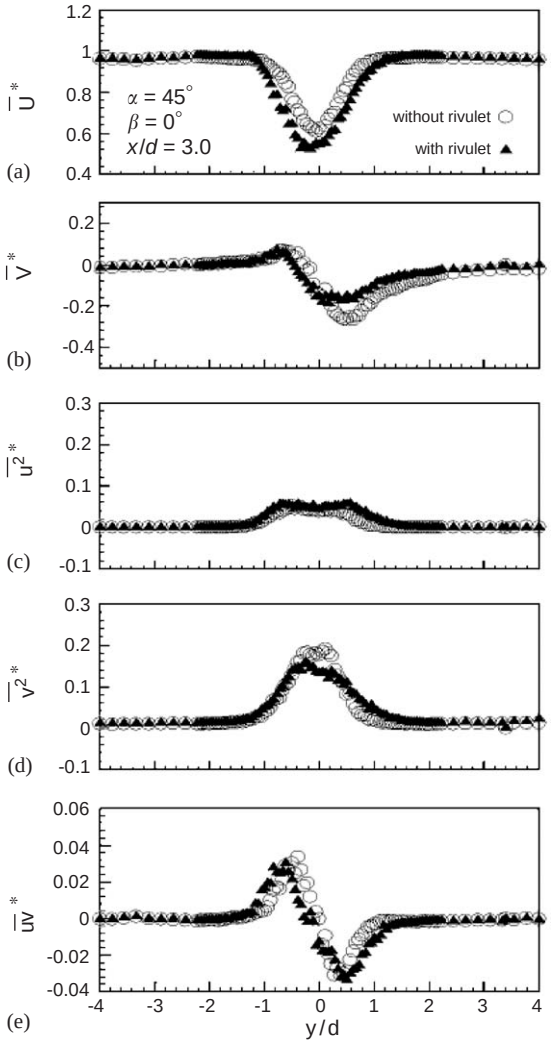

Fig. 7. Cross-flow distributions of mean velocity, Reynolds normal stresses and shear stress at $\alpha = 45^\circ$, $\beta = 0^\circ$, $x/d = 3.0$: (a) $\overline{U}^*$, (b) $\overline{V}^*$, (c) $\overline{u^2}^*$, (d) $\overline{v^2}^*$, (e) $\overline{uv}^*$; ○, without rivulets; ▲, with two running water rivulets located symmetrically at $\theta \approx 110^\circ$ and $\theta \approx -110^\circ$.

paper, an overbar denotes time averaging and an asterisk indicates normalization by U_∞ and/or d. As expected, the distributions at $\beta = 0^\circ$ (Fig. 7) are reasonably symmetrical or antisymmetrical about $y/d = 0$ in the absence of water rivulets. With running water rivulets and $\beta \neq 0^\circ$, the $\overline{U}^*$, $\overline{V}^*$ and $\overline{v^2}^*$ distributions display distinct asymmetry, apparently under the effect of the rivulets. The asymmetry is more appreciable at $\beta = 30^\circ$. This is not unexpected. Firstly, as earlier observed, the two water rivulets are asymmetrically located at $\beta \neq 0^\circ$. Secondly, the elliptical cross-section of the cylinder in the (x, y) plane is asymmetrical about the x-axis at $\beta \neq 0^\circ$ (Fig. 2).

Note that the wake at $\beta = 0^\circ$ displays asymmetry about $y/d = 0$, mainly in the $\overline{V}^*$ distribution, though not substantially (Fig. 7(b)). The observation could not be simply ascribed to experimental uncertainties in LDA measurements, which were estimated to be 3% for the mean velocity measurements (Section 2.3). In this case, the two rivulets are supposed to be statistically symmetrically formed about the leading stagnation point. However, given asymmetrical vortex shedding, as supported by the $\overline{uv}^*$ measurements (Fig. 7(e)), the two rivulets, which oscillate both circumferentially and axially, do not occur symmetrically at any instant, since their motions are connected to flow separation from the cable. Furthermore, the water released at the top end of the cylinder developed into two rivulets (Section 3), whose mass flow rates may not be identical. Consequently, the positions of the two water

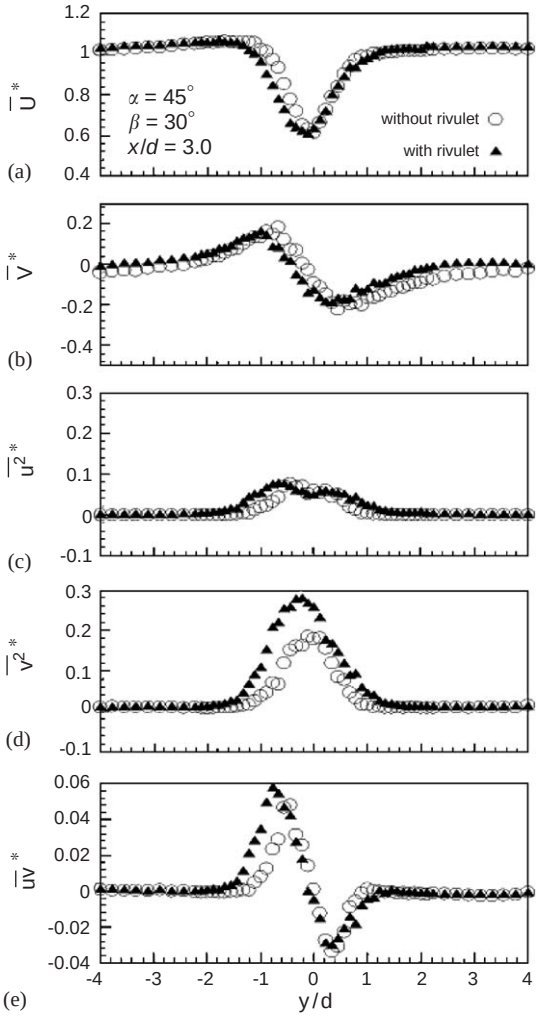

Fig. 8. Cross-flow distributions of mean velocity, Reynolds normal stresses and shear stress at $\alpha = 45^\circ$, $\beta = 30^\circ$, $x/d = 3.0$: (a) $\overline{U}^*$, (b) $\overline{V}^*$, (c) $\overline{u^2}^*$, (d) $\overline{v^2}^*$, (e) $\overline{uv}^*$; ○, without rivulets; ▲, with a leeward running water rivulet at $\theta \approx 55^\circ$ and a windward water rivulet at $\theta \approx -145^\circ$.

rivulets will deviate from symmetry about $y/d = 0$ since the mean circumferential rivulet location depends on the mass flow rates (e.g. Fig. 6). Both reasons may contribute to the observed the asymmetrical distribution in $\overline{V}^*$ (Fig. 7(b)).

At $\beta = 0^\circ$, the distributions of $\overline{U}^*$, $\overline{V}^*$, $\overline{u^2}^*$, $\overline{v^2}^*$ and $\overline{uv}^*$ with running water rivulets show appreciable deviation from those without rivulets (Fig. 7). The $\overline{u^2}^*$ (Fig. 7(c)) displays a twin peak distribution in both cases, though the two peaks are more pronounced and farther separated in the presence of water rivulets. This observation suggests that the presence of water rivulets results in larger lateral spacing between two rows of oppositely signed vortices than that without the rivulets, which is supported by the PIV data shown later. At $\beta = 30^\circ$ (Fig. 8), the running water rivulets produce a more significant deviation from the case without the rivulets than at $\beta = 0^\circ$, particularly on the cylinder side of $y/d < 0$, where the leeward rivulet occurs. The rivulets apparently lead to a significant increase in $\overline{u^2}^*$, $\overline{v^2}^*$ and $\overline{uv}^*$, which is consistent with an increased vortex strength. It was noted that the circumferential oscillation of the leeward rivulet is very significant, up to $\Delta\theta \approx \pm 15^\circ$, at $\beta = 30^\circ$, while both rivulets are quite steady, with little circumferential oscillation, at $\beta = 0^\circ$. The result points to the large circumferential oscillation of the leeward rivulet being mainly responsible for the significant variation in $\overline{U}^*$, $\overline{V}^*$, $\overline{u^2}^*$, $\overline{v^2}^*$ and $\overline{uv}^*$, which conforms to the Matsumoto et al. (2001a) proposition that the leeward water rivulet may control the aerodynamic instability. Note that the twin-peak distribution of $\overline{u^2}^*$ (Fig. 8(c)) is more evident at $\beta = 30^\circ$ than at $\beta = 0^\circ$ in the presence of the rivulets.

4.2. Drag and dominant frequencies

The drag coefficient C_D of a circular cylinder may be estimated by (Antonia and Rajagopalan, 1990)

$$C_D = 2\int_{-\infty}^{\infty} \frac{\overline{U}}{U_\infty}\left(\frac{U_\infty - \overline{U}}{U_\infty}\right)\mathrm{d}\left(\frac{y}{d}\right) + 2\int_{-\infty}^{\infty}\left(\frac{\overline{v^2} - \overline{u^2}}{U_\infty^2}\right)\mathrm{d}\left(\frac{y}{d}\right).$$

Thus, estimated C_D was 1.58 and 1.75 at $\beta = 0^\circ$ and 30°, respectively, with running water rivulets ($\alpha = 45^\circ$), 21% and 34% higher than their counterparts (1.31 at $\beta = 0^\circ$ and 1.30 at $\beta = 30^\circ$) in the absence of the water rivulets. This difference between the cases with and without running water rivulets cannot be ascribed to the experimental uncertainty, estimated to be $\pm 4\%$ based on repeated measurements, in determining C_D. The result is consistent with the violent rain–wind-induced structural vibration observed in the field. The enlarged difference at $\beta = 30^\circ$ in C_D between the cases with and without water rivulets further conforms to previous reports that the violent rain–wind-induced cable vibration tends to occur at $\beta = 20-60^\circ$ (Yoshimura et al., 1988; Flamand, 1995).

One remark is due here on the observed drag enhancement in the presence of water rivulets over the inclined cylinder. Bearman and Owen (1998) found that the introduction of wavy separation lines could suppress vortex shedding and hence result in a drag reduction of at least 30%. When projected into a plane normal to the wind, the present cylinder with water rivulets is also a wavy structure if the rivulets were considered as part of the structure. However, this 'wavy' structure does not suppress the drag, as Bearman and Owen's (1998) wavy structures did; instead, it does the opposite. It seems plausible that the presently observed drag increase could not be simply ascribed to the protuberance the rivulets posed. It is probably the movement of the water rivulets, in both axial and circumferential directions, that contributes to the enhanced drag. This assertion has yet to be verified in future investigations.

A hot film was placed at $x/d = 3$ and $y/d = 2.2$ ($z/d = 0$) behind the inclined cable to record fluctuating velocity time histories, from which the power spectra were produced. Fig. 9 presents the power spectral density function, E_u, weighted by the frequency f, of the fluctuating velocity, u, measured using the hotfilm with and without water rivulets formed on the cylinder at $\beta = 30^\circ$. This weighted spectrum, fE_u, provides a measure of the energy distribution with respect to frequency. A pronounced peak occurs at $f_s^* = f_s d/U_\infty \approx 0.23$ ($f_s \approx 45$ Hz) without rivulets and 0.33 ($f_s \approx 65$ Hz) with rivulets in fE_u, indicating an increase by 45% in the dominant vortex frequency in the wake. Note that the peak is less pronounced than that measured behind a cylinder normal to the incident flow (Zhou and Antonia, 1994), implying less quasi-periodical vortex shedding. Assuming a constant vortex shedding frequency, an increase in the effective height of cylinder due to the occurrence of rivulets should increase f_s^*. However, the observed percentage increase (43%) in f_s^* is far out of proportion of the effective height increase, which is estimated to be no more than 5%. The result suggests that the presence of the water rivulets has altered the dominant vortex frequency.

4.3. Flow structures

The flow structures in the (x, y)-plane and a vertical plane through the cylinder axis were captured by both flow visualization and PIV measurements. In general, the flow in the (x, y)-plane may display an alternate vortex street (Fig. 10(b)) or may not (Fig. 10(a)), that is, the vortex street occurs intermittently. For instance, among three hundred flow-visualization images examined at $\beta = 0^\circ$, about 30% of them display a vortex street in the absence of water rivulets, but this percentage increases to about 60% in the presence of water rivulets. In the vertical plane through the cylinder axis, the turbulent organized structures are also evident. For example, at $\beta = 0^\circ$, where this plane overlaps with the (x, z)-plane, the flow structure shown in Fig. 11(a) is consistent with the quasi-periodical flow separation from the cylinder. Fig. 11(b) further shows mushroom-like structures, which are not so evident at $\beta = 30^\circ$ (not shown) and will be further discussed later along with the vorticity contours.

Figs. 12 and 13 compare vorticity contours, $\omega_z^* = \omega_z d/U_\infty$, measured in the ($x$, y)-plane using the PIV technique, with and without running water rivulets at $\beta = 0^\circ$ and 30° ($\alpha = 45^\circ$), respectively. The contours are rather typical for the intermittently observed vortex street. A number of observations can be made based on the data. Firstly, the oppositely signed shear layers may separate symmetrically from the cylinder, as illustrated in Fig. 12(a). The observation is in distinct contrast to alternate vortex shedding from a circular cylinder normal to incident flow. The symmetrical flow separation occurs more frequently in the absence of water rivulets; at $\beta = 30^\circ$, this flow structure is recognized in about 25% of images examined without water rivulets but only 15% with the rivulets. The sample size consists of 300 images in each case. It is suspected that this difference could contribute to the more violent cable vibration in the presence of

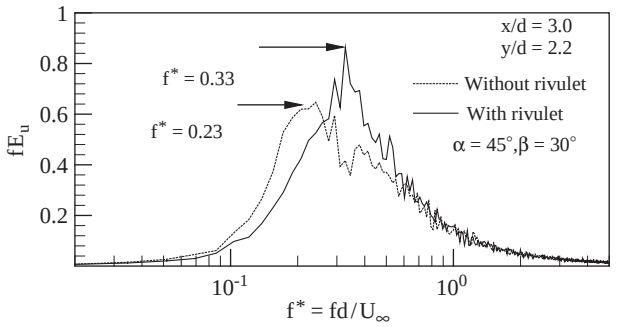

Fig. 9. Weighted u-spectrum, fE_u, of the fluctuating velocity u measured at $x/d = 3.0$ and $y/d = 2.2$, $\alpha = 45^\circ$, $\beta = 30^\circ$ and $U_\infty = 9.0\,\mathrm{m/s}$: ----, without rivulets; —, with a leeward running water rivulet at $\theta \approx 55^\circ$ and a windward rivulet at $\theta \approx -145^\circ$.

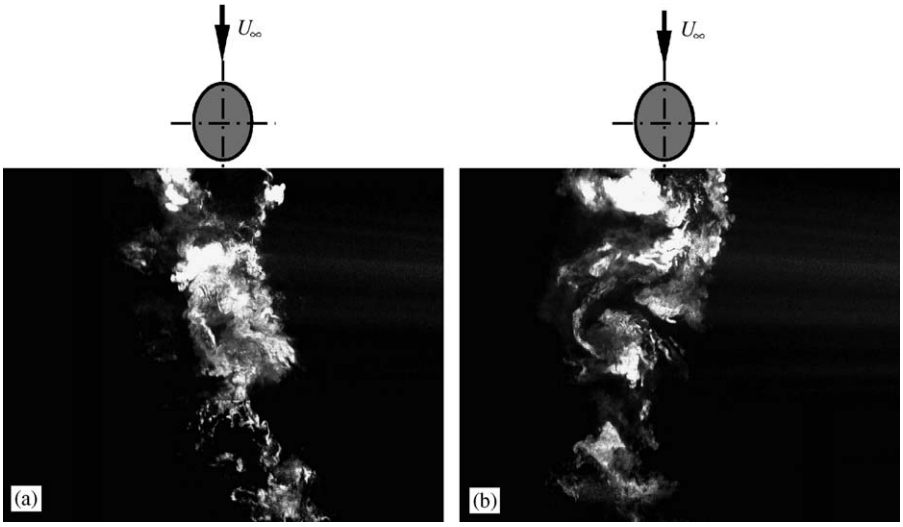

Fig. 10. Typical flow patterns behind the inclined cylinder at $\alpha = 45^\circ$, $\beta = 0^\circ$ and $\mathrm{Re} = 27\,000$ ($U_\infty = 9\,\mathrm{m/s}$) obtained in the wind tunnel in the horizontal (x, y) plane: (a) without water rivulet; (b) with two running water rivulets. Flow is downwards.

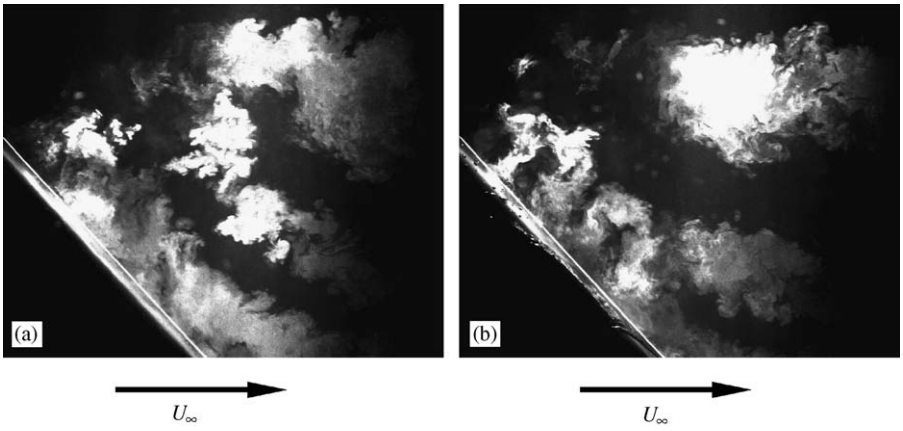

Fig. 11. Typical flow patterns behind the inclined cable at $\alpha = 45^\circ$, $\beta = 0^\circ$ and $\mathrm{Re} = 27\,000$ ($U_\infty = 9\,\mathrm{m/s}$) obtained in the wind tunnel in the vertical plane through the cylinder axis: (a) without water rivulet; (b) with two running water rivulets. Flow is from left to right.

the water rivulets. Secondly, as β increases from 0° to 30°, there is a marked increase in the peak vorticity of vortices with water rivulets running (Figs. 12(b) and 13(b)); the averaged maximum magnitude, estimated from three hundred images, rises by about 50%. Meanwhile, the vortex sizes are rather comparable in the two cases. It may be inferred that the vortex strength has been significantly increased from $\beta = 0°$ to 30°. This increase is apparently linked to the increase in C_D from 0° to 30° and probably attributed to an effective cylinder height larger at $\beta = 30°$ than at $\beta = 0°$ (refer to Fig. 2). The result may also provide an explanation for the observation that the rain–wind-induced vibrations occur often at a yaw angle of $\beta = 20-60°$ (Yoshimura et al., 1988; Flamand, 1995). In the absence of water rivulets, however, the averaged maximum vorticity magnitude changes little between the $\beta = 0°$ and 30° cases. See Figs. 12(a) and 13(a) for examples of instantaneous vorticity contours. Both are also quite comparable with that with water rivulets at $\beta = 0°$ (Fig. 12(b)). Thirdly, the lateral spacing between oppositely signed vortices enlarges appreciably in the presence of running water rivulets, compared with the case without the rivulets, which is internally consistent with the twin-peak distribution of $\overline{u^{2*}}$ (Figs. 7(c) and 8(c)). This is probably due to the increased effective cylinder height.

Insight into the three-dimensional aspects of flow separation from the cylinder may be gained by examining PIV-measured vorticity contours in the vertical plane through the cylinder axis, as shown in Figs. 14 and 15. This plane overlaps with the (x, z)-plane at $\beta = 0°$ but not at $\beta = 30°$. Note that the abscissa in Fig. 15 is denoted by x_β. Use was made of ω_y and ω to represent the measured vorticity in the former and the latter, respectively. Interestingly, the ω_y concentrations (Fig. 14) in close proximity of the cylinder tend to occur alternately in sign along the axial direction, with or without the water rivulets, and appear quite similar to the longitudinal vortices observed behind a cylinder normal to incident flow by Wu et al. (1994). The structures apparently correspond to the mushroom structures seen in Fig. 11(a). The alternately signed structures seem to be best captured in the (x, z)-plane; they are less evident at $\beta = 30°$ (Fig. 15) since the plane of PIV images is not parallel to the (x, z)-plane. Due to the complexities of the present three-dimensional flow, further investigations are needed to clarify the interaction between the longitudinal and Karman vortices.

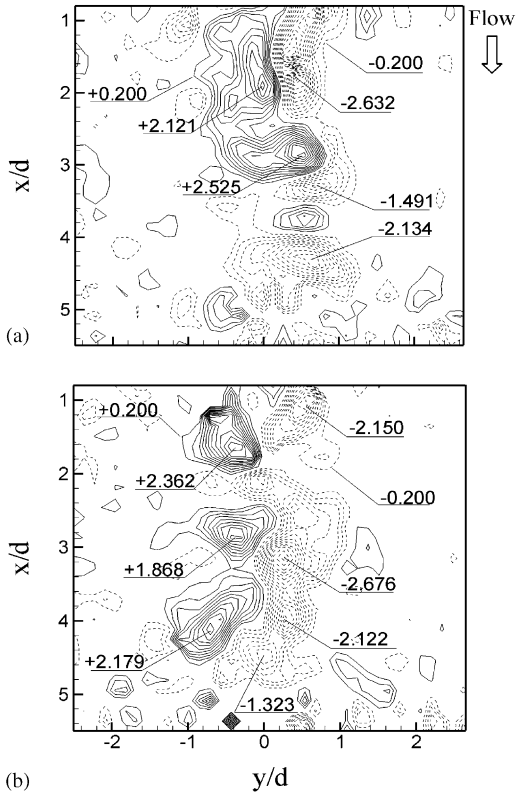

Fig. 12. Instantaneous vorticity contours $\omega_z^* = \omega_z d/U_\infty$ obtained from PIV measurements at $\alpha = 45°$, $\beta = 0°$ and $\mathrm{Re} = 11\,400$ ($U_\infty = 9\,\mathrm{m/s}$) in the horizontal ($x$, y) plane: (a) without water rivulet; (b) with two running water rivulets. Flow is downwards.

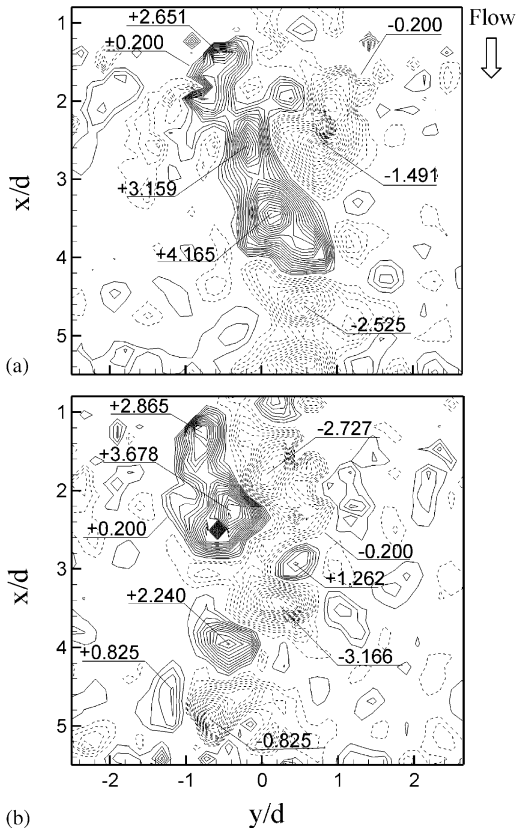

Fig. 13. Instantaneous vorticity contours $\omega_z^* = \omega_z d/U_\infty$ obtained from PIV measurements at $\alpha = 45^\circ$, $\beta = 30^\circ$ and $\mathrm{Re} = 11\,400$ ($U_\infty = 9\,\mathrm{m/s}$) in the horizontal ($x$, y) plane: (a) without water rivulet; (b) with two running water rivulets. Flow is downwards.

5. Discussion

A scenario of the rain–wind-induced cable vibration may be proposed based on the present data as well as those in the literature. At $\beta = 0^\circ$, the vortex street occurs intermittently and the vortex strength is relatively weak, although Verwiebe and Ruscheweyh (1998) did report the rain–wind-induced cable vibration in the case of an almost vertical cable. Thus, it is difficult to induce violent cable vibration. As β increases from 0° to 30°, the strength of vortices rises by up to 60%. In the presence of running water rivulets, shear layer separation from the cylinder tends to be antisymmetrical and lateral spacing between the oppositely signed vortices enlarges. All these could contribute to an enhanced excitation force on the cylinder, which compromises the significant rise in the mean drag on the cylinder. However, these may not be adequate to account for the violent cable vibration observed in engineering.

Zhang et al. (2004) used piezoelectric ceramic actuators to perturb one surface of a square cylinder in a cross-flow. The cylinder was spring-supported at both ends. Vortex shedding from the cylinder was in synchronization with the natural frequency of the fluid–structure system. When the surface perturbation, albeit very small in amplitude (only 0.6% of the cylinder height), was made in phase with vortex shedding or the natural frequency of the system through a feedback control system, the vortex strength was doubled and the fluid–structure system damping was significantly reduced. Subsequently, the cylinder oscillation amplitude was greatly amplified. The present data reconfirm previous reports that running water rivulets along the cylinder oscillate circumferentially around the flow separation line. The oscillation is up to $\pm 15^\circ$ at $\beta = 30^\circ$. Naturally, the rivulets act to perturb or impose a perturbation force on the flow separation. Presumably, their oscillating frequency is the same as the vortex shedding frequency. Given the two frequencies are synchronized with the natural frequency of the fluid-cylinder system (or its harmonics), vortex shedding can be greatly enhanced and the fluid-cylinder system damping will be considerably reduced. As a consequence, the excitation force and hence the cylinder vibration amplitude may be greatly amplified. Since the present cylinder was

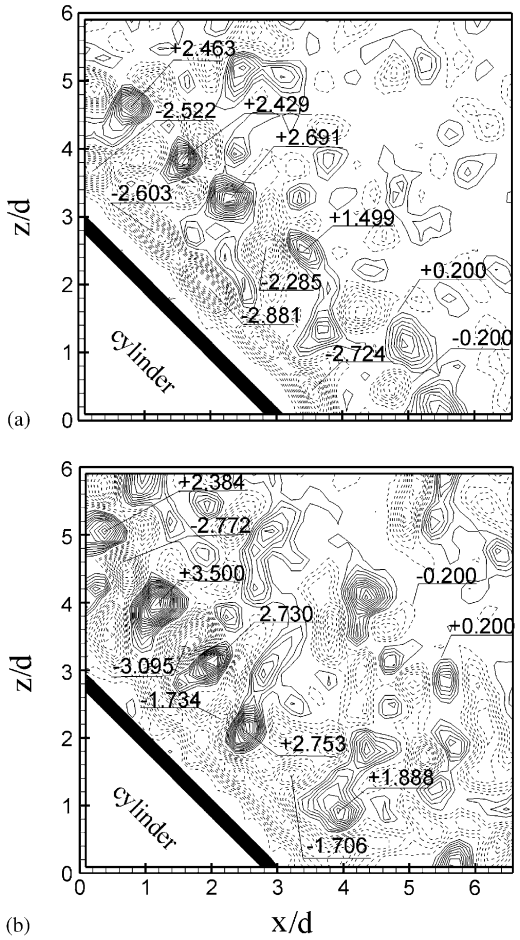

Fig. 14. Instantaneous vorticity contours $\omega_y^* = \omega_y d/U_\infty$ obtained in a vertical plane through the cylinder axis from PIV measurements at $\alpha = 45^\circ$, $\beta = 0^\circ$ and $\mathrm{Re} = 11\,400$ ($U_\infty = 9\,\mathrm{m/s}$): (a) without water rivulet; (b) with two running water rivulets.

very rigid and fix-supported, implying a large damping and negligibly small vibration, the vortex shedding or rivulet oscillation frequency cannot be synchronized with the system natural frequency. Thus, the running water rivulets could only have a very limited effect on the vortex shedding strength.

6. Conclusions

The formation of running water rivulets on an inclined stationary cylinder subjected to cross wind and its effects on the near wake were experimentally investigated. The following conclusions may be drawn from the investigation:

(i) One windward (lower) and one leeward (upper) water rivulets were formed on the cylinder at $\alpha = 45^\circ$ and $0^\circ \leqslant \beta \leqslant 90^\circ$ for $U_\infty = 8-15\,\mathrm{m/s}$. The rivulet position and behavior depend on the running water rate Q, wind speed U_∞, and cylinder yaw angle β. Both water rivulets occur around the flow separation line. As U_∞ increases, the rivulets tend to climb up the cylinder surface, possibly due to the dependence of flow separation point on Re.
(ii) Both water rivulets oscillate circumferentially, which is connected to the nature of the oscillating flow separation point associated with circular or elliptical cross-section structures. The oscillation is rather small at $\beta = 0^\circ$, but up to $\pm 15^\circ$ at $\beta = 30^\circ$. The leeward rivulet appears to be pseudo-sinusoidal with an axial wavelength of about $2d$, which is probably linked to an axial vortex cell wavelength.

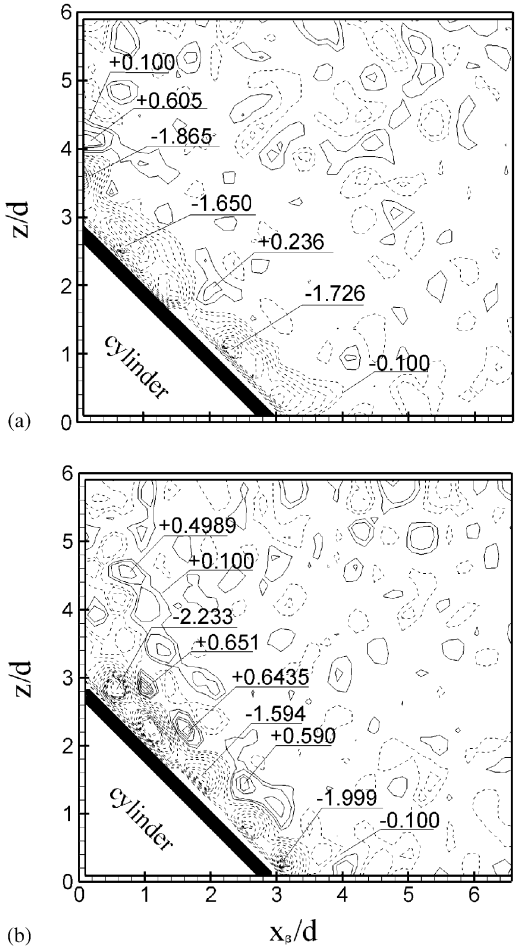

Fig. 15. Instantaneous vorticity contours $\omega^* = \omega d/U_\infty$ obtained in a vertical plane through the cylinder axis from PIV measurements at $\alpha = 45^\circ$, $\beta = 30^\circ$ and $\mathrm{Re} = 11\,400$ ($U_\infty = 9\,\mathrm{m/s}$): (a) without water rivulet; (b) with two running water rivulets.

(iii) The quasi-periodical vortex street occurs intermittently in the (x, y)-plane, and tends to occur more frequently in the presence of running water rivulets. The vortices may be antisymmetrically or symmetrically arranged, unlike those behind a cylinder normal to the incident flow, which are predominantly antisymmetric about the flow centreline. Nevertheless, the antisymmetric vortex street occurs more frequently with running water rivulets than without. Meanwhile, there appear mushroom-like structures in close proximity of the inclined cylinder in the (x, z)-plane, which are likely to result from the three-dimensional flow separation from the cylinder, that is, the separation line is pseudo-sinusoidal.

(iv) The vortex strength increases up to 60% as β changes from 0° to 30°. The result is consistent with the report that violent rain–wind-induced cable vibrations tend to occur for $\beta > 20^\circ$. At $\beta = 30^\circ$, the cross-stream distributions of the mean velocity $\overline{U}^*$, $\overline{V}^*$ and the Reynolds stresses $\overline{u^2}^*$, $\overline{v^2}^*$ and $\overline{uv}^*$ vary considerably in the presence of running water rivulets along the cylinder. Accordingly, the drag force on the cylinder, estimated based on $\overline{U}^*$, $\overline{u^2}^*$ and $\overline{v^2}^*$, increases significantly, compared with that in the absence of the rivulets. This increase and the violent rain–wind-induced vibration could be well connected. The formation of water rivulets on the cylinder surface increases appreciably the normalized dominant frequencies in the near-wake.

(v) It is proposed that the large circumferential oscillation at large β of the water rivulets may act to perturb the flow separation from the cylinder. When the perturbation frequency that should be the same as the vortex shedding frequency coincides with the natural frequency of the fluid-cable system (or its harmonics), the system damping may be significantly reduced, and vortex shedding and hence structural vibration could be greatly amplified. This proposition has yet to be verified by future investigations.

Acknowledgments

Yu Zhou wishes to acknowledge support given to him by the Research Grants Council of the Government of the HKSAR through Grants PolyU 5316/03E and by the Central Research Grant of The Hong Kong Polytechnic University through Grant G-YD21.

References

Achenbach, E., 1968. Distribution of local pressure and skin friction around a circular cylinder in a cross-flow up to $Re = 5 \times 10^6$. Journal of Fluid Mechanics 34, 625–639.

Antonia, R.A., Rajagopalan, S., 1990. Determination of drag of a circular cylinder. AIAA Journal 28, 1833–1834.

Bearman, P.W., Owen, J.C., 1998. Special brief note—reduction of bluff-body drag and suppression of vortex shedding by the introduction of wavy separation lines. Journal of Fluids and Structures 12, 123–130.

Bosdogianni, A., Olivari, D., 1996. Wind- and rain-induced oscillations of cables of stayed bridges. Journal of Wind Engineering and Industrial Aerodynamics 64, 171–185.

Chen, S.S., 1987. Flow-Induced Vibration of Circular Cylindrical Structures. Hemisphere Publishing Corporation, Washington.

Dwyer, H.A., McCroskey, W.J., 1973. Oscillating flow over a cylinder at large Reynolds number. Journal of Fluid Mechanics 61, 753–767.

Flamand, O., 1995. Rain–wind induced vibration of cables. Journal of Wind Engineering and Industrial Aerodynamics 57, 353–362.

Higuchi, H., Kim, H.J., Farell, C., 1989. On flow separation and reattachment around a circular cylinder at critical Reynolds numbers. Journal of Fluid Mechanics 200, 149–171.

Hikami, Y., Shiraishi, N., 1988. Rain–wind induced vibrations of cables in cable stayed bridges. Journal of Wind Engineering and Industrial Aerodynamics 29, 409–418.

King, R., 1977. A review of vortex shedding research and its application. Ocean Engineering 4, 141–171.

Matsumoto, M., Saitoh, T., Kitazawa, M., Shirato, H., Nishizaki, T., 1995. Response characteristics of rain–wind induced vibration of stay-cables of cable-stayed bridges. Journal of Wind Engineering and Industrial Aerodynamics 57, 323–333.

Matsumoto, M., Daito, Y., Kanamura, T., Shigemura, Y., Sakuma, S., Ishizaki, H., 1998. Wind-induced vibration of cables of cable-stayed bridges. Journal of Wind Engineering and Industrial Aerodynamics 74–76, 1015–1027.

Matsumoto, M., Yagi, T., Shigemura, Y., Tsushima, D., 2001a. Vortex-induced cable vibration of cable-stayed bridges at high reduced wind velocity. Journal of Wind Engineering and Industrial Aerodynamics 89, 633–647.

Matsumoto, M., Yagi, T., Shigemura, Y., Tsushima, D., 2001b. Rain–wind induced vibration of inclined cables at limited high reduced wind velocity region. In: Proceedings of the Fifth Asia-Pacific Conference on Wind Engineering, Kyoto, pp. 101–104.

Ohshima, K., 1987. Aerodynamic stability of the cables of a cable-stayed bridge subject to rain (a case study of the Ajigawa bridge). In: Proceedings of US-Japan Joint Seminar on Natural Resources, pp. 324–336.

Ramberg, S.E., 1983. The effects of yaw and finite length upon the vortex wakes of stationary and vibrating circular cylinders. Journal of Fluid Mechanics 128, 81–107.

Thomson, K.D., Morrison, D.F., 1971. The spacing, position and strength of vortices in the wake of slender cylindrical bodies at large incidence. Journal of Fluid Mechanics 50, 751–783.

Verwiebe, C., Ruscheweyh, H., 1998. Recent research results concerning the exciting mechanisms of rain–wind-induced vibrations. Journal of Wind Engineering and Industrial Aerodynamics 74–76, 1005–1013.

Wianecki, J., 1979. Cables wind excited vibrations of cable stayed bridge. In: Proceedings of the Fifth International Conference on Wind Engineering, vol. l.2, pp. 1381–1393.

Wu, J., Sheridan, J., Welsh, M.C., Hourigan, K., Thompson, M., 1994. Longitudinal vortex structures in a plane wake. Physics of Fluids 6, 2883–2885.

Xu, S.J., Zhou, Y., So, R.M.C., 2003. Reynolds number effects on the flow structure behind two side-by-side cylinders. Physics of Fluids 15, 1214–1219.

Yamaguchi, H., 1990. Analytical study on growth mechanism of rain vibration of cables. Journal of Wind Engineering and Industrial Aerodynamics 33, 73–80.

Yoshimura, T., Tanaka, T., Sasaki, N., Nakatani, S., Higa, S., 1988. Rain–wind induced vibration of the cables of the Aratsu Bridge. In: Proceedings of the 10th National Conference on Wind Engineering, Tokyo, pp. 127–132.

Zhang, M.M., Cheng, L., Zhou, Y., 2004. Closed-loop-controlled vortex shedding from a flexibly supported square cylinder under different schemes. Physics of Fluids 16, 1439–1448.

Zhou, Y., Antonia, R.A., 1994. Effect of initial conditions on structures in a turbulent near-wake. AIAA Journal 32, 1207–1213.

Zhou, Y., Wang, Z.J., So, R.M.C., Xu, S.J., Jin, W., 2001. Free vibrations of two side-by-side cylinder in a cross flow. Journal of Fluid Mechanics 443, 197–229.